

---

# Intrinsic PAPR for Point-level 3D Scene Albedo and Shading Editing

---

Alireza Moazeni, Shichong Peng, Ke Li  
APEX Lab  
School of Computing Science  
Simon Fraser University  
{sam62, shichong\_peng, keli}@sfu.ca

## Abstract

Recent advancements in neural rendering have excelled at novel view synthesis from multi-view RGB images. However, they often lack the capability to edit the shading or colour of the scene at a detailed point-level, while ensuring consistency across different viewpoints. In this work, we address the challenge of point-level 3D scene albedo and shading editing from multi-view RGB images, focusing on detailed editing at the point-level rather than at a part or global level. While prior works based on volumetric representation such as NeRF struggle with achieving 3D consistent editing at the point level, recent advancements in point-based neural rendering show promise in overcoming this challenge. We introduce “Intrinsic PAPR”, a novel method based on the recent point-based neural rendering technique Proximity Attention Point Rendering (PAPR). Unlike other point-based methods that model the intrinsic decomposition of the scene, our approach does not rely on complicated shading models or simplistic priors that may not universally apply. Instead, we directly model scene decomposition into albedo and shading components, leading to better estimation accuracy. Comparative evaluations against the latest point-based inverse rendering methods demonstrate that Intrinsic PAPR achieves higher-quality novel view rendering and superior point-level albedo and shading editing.

## 1 Introduction

Recent advancements in point-based neural rendering methods [10, 20, 38, 30, 7, 32] have gained significant attention due to their efficiency in rendering compared to volumetric representations like NeRF [17]. These methods have showcased impressive rendering quality, particularly in novel view synthesis tasks. However, they often lack the capability for intuitive editing tasks such as altering shading or colour within the scene. On the other hand, current image intrinsic decomposition techniques [16, 34, 15, 5, 1] excel at pixel-level albedo and shading editing for 2D images, demonstrating the ability to generalize across diverse scenes. Nevertheless, extending such detailed editing capabilities to 3D scenes that is consistent across different viewpoints remains a challenge. We term this challenge as “point-level 3D scene albedo and shading editing”, and this work is dedicated to addressing this problem.

To enable albedo and shading editing in a 3D scene, a common approach involves inverse rendering, where the scene is decomposed into its geometry, reflectance, and illumination. However, due to the potential for multiple solutions for each component that yield the same rendered images, inverse rendering is considered highly ill-posed. Consequently, these methods often depend on prior assumptions for each of the scene decomposition component, but these assumptions may not hold universally, thereby limiting their estimation accuracy in practice.

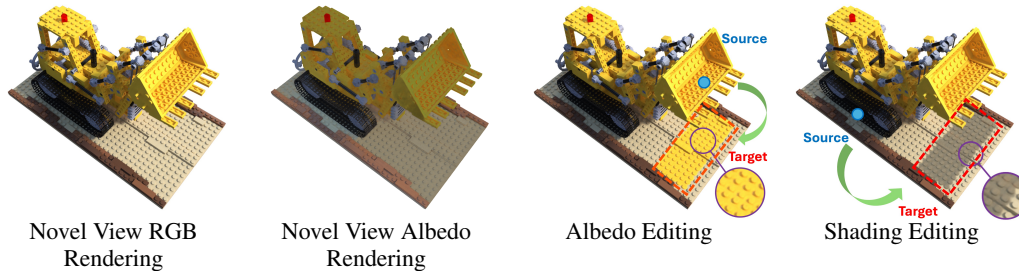


Figure 1: We introduce Intrinsic PAPR, a novel method for point-level 3D scene albedo and shading editing. By leveraging the recent point-based rendering technique, PAPR, our method models the scene decomposition into albedo and shading components. This enables detailed, point-level albedo and shading edits that remain consistent across different viewpoints.

In this paper, we choose a simpler approach to achieve 3D scene albedo and shading editing by directly modeling the intrinsic decomposition of the scene into shading and albedo components. We leverage a recent image intrinsic decomposition model [1] to extract the albedo of the scene image at each viewpoint, which serves as our supervision target. For scene representation, we build upon the recent Proximity Attention Point Rendering (PAPR) technique [32], known for its proficiency in learning a parsimonious representation of the scene using point cloud. To capture local scene appearance information, PAPR learns a feature vector for each point.

We develop a new approach based on PAPR by decomposing the dimensions of the feature vector for each point to model shading and albedo separately, and we dub our method “Intrinsic PAPR”. During testing, Intrinsic PAPR enables albedo and shading editing by changing the shading or albedo feature vector at each point. In particular, our point-based representation allows us to achieve such editing at a point-level, thereby achieving detailed and 3D consistent editing of the scene, as shown in Figure 1. We evaluate our method against the latest point-based inverse rendering baselines on synthetic and real-world scenes, demonstrating that Intrinsic PAPR achieves higher-quality novel view rendering and superior point-level shading and albedo transfer compared to these baselines. In summary, our contributions are as follows:

1. We introduce Intrinsic-PAPR, which models the decomposition of the scene into albedo and shading.
2. We showcase our method’s ability to achieve point-level albedo and shading editing.
3. We outperform the latest point-based inverse rendering baselines in terms of novel view rendering quality and point-level 3D scene albedo and shading editing.

## 2 Related Work

### 2.1 Neural Scene Representation

In recent years, there has been a surge in interest in using neural networks for novel view synthesis from multi-view RGB images [17, 28, 18, 2, 25, 7, 32]. The 3D neural representations used by these neural rendering methods can be broadly categorized into volumetric and surface representations. Volumetric representations, exemplified by NeRF [17], exhibit impressive rendering quality but suffer from high computational costs due to the need to evaluate multiple samples along each ray for rendering. Furthermore, achieving precise point-level scene editing in volumetric representations requires changing scene information across all spatial regions corresponding to the target 3D area, presenting a non-trivial challenge.

In contrast, surface representations can render with much fewer samples, leading to increased efficiency. Recent advancements in point-based neural renderers [10, 20, 38, 30, 7, 32] have gained increasing attention due to their high rendering quality and efficiency. These methods store local scene information at each point, making them well-suited for precise point-level editing by modifying the information in the points at the desired region. Among these methods, splat-based techniques [10, 38, 30, 7] use radial basis functions to calculate point contributions to rays and combine the scene

information stored at each point into the output. However, editing one splat does not influence neighbouring splats due to its discrete nature, potentially causing unnatural appearance transitions between edited splats and their neighbours.

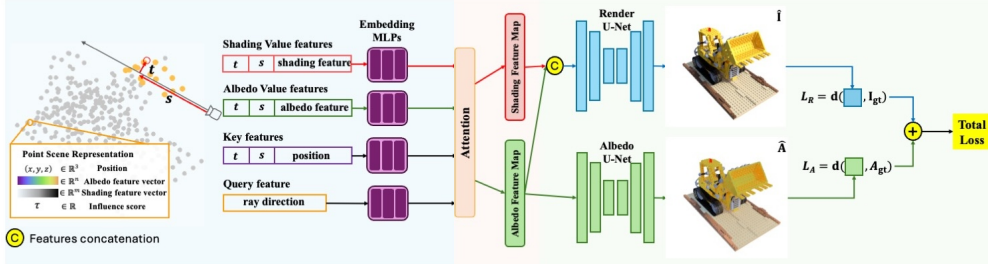
On the other hand, attention-based methods [20, 32] interpolate information stored at neighbouring points around each pixel for rendering. This approach ensures smooth appearance transitions between edited points and their neighbours. In particular, Proximity Attention Point Rendering (PAPR) [32] stands out for its ability to learn parsimonious point cloud from scratch. In this work, we adopt PAPR as our neural scene representation.

## 2.2 Intrinsic Decomposition

The field of image intrinsic decomposition has a rich history, aiming to decompose images into reflectance and shading components. Early methods focused on predicting ordinal relationships between the albedos of pixel pairs [19, 35, 37], while later approaches directly regress to continuous shading and albedo values [12, 16, 22, 34, 36, 5]. However, training models that generalize well to real-world imagery remains a challenge due to domain gaps between synthetic datasets used for supervised training and real-world data. To bridge this gap, Careaga and Aksoy [1] combine synthetic data pretraining with real-world multi-illumination data to generate dense pseudo-ground-truth intrinsic components for further training, thereby bridging the intrinsic decomposition generalization gap.

While the aforementioned methods focus on intrinsic decomposition of 2D images, there is a growing interest in adopting neural rendering for modelling intrinsic decomposition in 3D scenes. IntrinsicNeRF [27] uses an iterative reflectance clustering method for unsupervised reconstruction of albedo and shading. LitNeRF [21] combines volume rendering with traditional mesh reconstruction methods for few-view intrinsic decomposition modelling of human faces. Similar to our approach, Point-Net [24] encodes intrinsic components into a point cloud, but their setup requires RGB-D images for point cloud generation, whereas our method can train from scratch using only RGB images.

Recent works [23, 29, 33, 6, 3, 14] also explore combining neural rendering with inverse rendering, which involves more sophisticated scene models with geometry, reflectance, and illumination components. While this approach offers increased modelling capacity, it introduces more degrees of freedom in the parameter space and relies on priors for different components to find solutions. These simple priors may not universally hold, which limits their estimation accuracy in practice.



(a) Ray-dependent Point Embedding      (b) Proximity Attention      (c) Point Feature Rendering

Figure 2: An overview of the rendering pipeline. Each point in our scene representation contains a spatial position, albedo, shading feature vectors, and an influence score. (a) Ray-dependent embeddings are generated for each point, incorporating the key, albedo value, and shading value, along with the ray direction forming the query, which together serve as inputs to the attention model. (b) The attention model uses the key and query to select points and combine their albedo and shading values, producing corresponding feature maps. (c) The albedo feature map is fed to an albedo feature renderer (green) to generate the albedo image. Both shading and albedo feature maps are input to a separate feature renderer (blue) for generating the final colour image output. The model is trained end-to-end with supervision on both the albedo output and the colour image output.

### 3 Method

#### 3.1 Preliminaries: Intrinsic Decomposition

Intrinsic image decomposition is a fundamental mid-level vision problem that aims to separate an image into reflectance (albedo) and shading components:

$$I = A * S \tag{1}$$

Here, the albedo component represents the illumination independent reflectance properties of the surface materials, while the shading component captures the scene’s illumination effects.

In comparison to inverse rendering (IR), which aims for a more detailed decomposition of scenes into geometry, reflectance, and illumination, intrinsic decomposition (ID) is a simpler approach with fewer parameters to estimate. This brings several benefits: (i) IR methods typically rely on simplistic prior assumptions for each decomposition component due to the larger free parameter space, and these assumptions may not hold in all cases, limiting their estimation accuracy in practice; (ii) the bias-variance trade-off suggests that simpler models can potentially achieve higher estimation accuracy on unseen data, which is crucial for better novel view synthesis. Additionally, extensive prior research on ID has resulted in pretrained models capable of directly extracting albedo and shading components, demonstrating strong generalizability across various synthetic and real-world data. In this work, we leverage the pretrained model from [1] to obtain the intrinsic components for the images of a 3D scene. These extracted albedo images then serve as supervision ground truths for the albedo components of the scene.

#### 3.2 Choice of Scene Representation

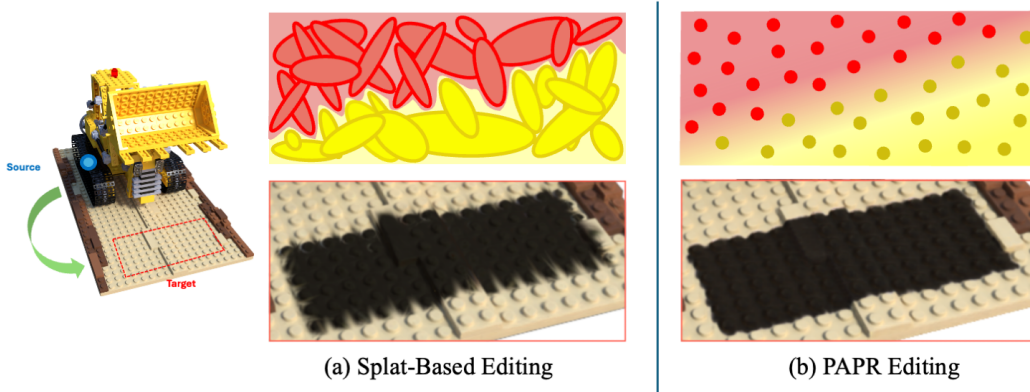


Figure 3: Illustrative comparison between splat-based renderers and attention-based renderers like PAPR. (a) Splat-based methods render scene appearance using information stored at discrete splats. Due to their discrete nature, changes made to splats on one side do not influence those on the other side, resulting in an abrupt transition at the boundary. (b) PAPR renders appearance through interpolation among points. The interpolated appearance between edited points on one side and unedited ones on the other side naturally creates a smooth transition.

Our approach builds on point-based 3D scene representations. These representations encode local scene appearance information at each point, which makes them ideal for achieving detailed point-level editing tasks. Given the challenge of producing realistic albedo and shading editing results, it necessitates a suitable point-based renderer.

There are two main classes of point-based renderers: splat-based renderers and attention-based renderers. In splat-based renderers [10, 38, 30, 7], the points are represented as primitives such as disks or Gaussian kernels, and the total contribution of all primitives intersecting the given ray forms rendering output at the ray. In contrast, attention-based methods, such as PAPR [32] interpolate the nearby points around the given ray to produce its rendering output.

To achieve realistic point-level albedo and shading editing, a smooth transition in appearance from the edited region and the surroundings is important. In splat-based approaches, each primitive operates independently, leading to potential abrupt transitions between edited splats and surrounding areas. As

illustrated in Figure 3, in comparison, PAPR does not suffer from this limitation and can produce a smooth transition between the edited region and its surroundings through interpolation; therefore, we choose PAPR as our scene representation.

### 3.3 Overview: Proximity Attention Point Rendering (PAPR)

PAPR [32] uses multi-view RGB images and corresponding camera poses to jointly learn a point-based scene representation along with an attention-based differentiable renderer. The scene representation includes a collection of 3D points denoted by  $P = \{(\mathbf{p}_i, \mathbf{u}_i, \tau_i)\}_{i=1}^N$ , where  $N$  is the total number of points, each associated with a location  $\mathbf{p}_i \in \mathbb{R}^3$ , a feature vector  $\mathbf{u}_i \in \mathbb{R}^d$  that encodes local scene appearance information, and an influence score  $\tau_i \in \mathbb{R}$ .

To render an image with a resolution of  $H \times W$  given a camera pose  $\mathcal{C}$ , PAPR shoots rays from the camera towards each pixel. At each ray, PAPR uses an attention mechanism to calculate the contribution of each point based on their distances to the ray, and combines their features into a feature map  $F_{\mathcal{C}} \in \mathbb{R}^{H \times W \times d_{\text{feat}}}$ . This feature map is then fed through a U-Net renderer to produce the output rendering. The whole pipeline is end-to-end differentiable, which can be trained by the following reconstruction loss:

$$\mathcal{L}_{\text{recon}} = d(\hat{\mathbf{I}}, \mathbf{I}_{gt}) \quad (2)$$

Here,  $\hat{\mathbf{I}}$  represents the rendered image,  $\mathbf{I}_{gt}$  represents the ground truth image, and  $d(\cdot, \cdot)$  is a weighted combination of mean squared error (MSE) and LPIPS [31] distance. For more details, please refer to the original paper [32].

### 3.4 Intrinsic PAPR

To model the intrinsic decomposition of a 3D scene into albedo and shading components, we partition the dimensions of the point feature vector into two orthogonal components. One component models the albedo, capturing the reflectance properties, while the other component models the shading, capturing the scene’s illumination effects. This design allows each point to store separate albedo and shading information while retaining all local scene details, which is essential for subsequent editing applications.

Specifically, our representation is denoted as  $P = \{(\mathbf{p}_i, \mathbf{a}_i, \mathbf{h}_i, \tau_i)\}_{i=1}^N$ , where  $\mathbf{a}_i \in \mathbb{R}^n$  represents the albedo feature vector and  $\mathbf{h}_i \in \mathbb{R}^m$  represents the shading feature vector for each point. These two feature vectors serve as inputs to their corresponding value branches in the attention mechanism, producing an albedo feature map  $A_{\mathcal{C}} \in \mathbb{R}^{H \times W \times d_{\text{albedo}}}$  and a shading feature map  $S_{\mathcal{C}} \in \mathbb{R}^{H \times W \times d_{\text{shading}}}$  using the attention weights.

To render the output colour image  $\hat{\mathbf{I}}$ , we concatenate the albedo and shading feature maps along the feature dimension and pass the combined feature map through a U-Net-based renderer. Additionally, we feed the albedo feature map through a separate U-Net-based renderer to produce an albedo image  $\hat{\mathbf{A}}$  of the scene. Figure 2 provides an illustration of the overall pipeline.

To train our model for modeling the intrinsic components, one approach could be to supervise both the albedo image and the predicted shading. However, areas with albedo values close to 0 (e.g., black or near-black regions) can lead to arbitrary shading values due to the formulation in Equation 1. Direct supervision of predicted shading might therefore result in incorrect values, adversely affecting shading prediction accuracy. Hence, we opt to implicitly learn the shading feature by supervising only the albedo image and the predicted colour image.

Specifically, we jointly optimize all parameters in our model by minimizing the distance metric  $d(\cdot, \cdot)$  between the rendered colour and albedo images and their corresponding ground truth images:

$$\mathcal{L} = d(\hat{\mathbf{I}}, \mathbf{I}_{gt}) + d(\hat{\mathbf{A}}, \mathbf{A}_{gt}) \quad (3)$$

Here, we use the same distance metric  $d(\cdot, \cdot)$  as PAPR [32].

**Training Details** We set hyperparameters as follows:  $m = n = 32$ ,  $d_{\text{albedo}} = d_{\text{shading}} = 16$ . We train our model using Adam optimizer [8] with a mini-batch size of 1 for 250,000 iterations training on a single NVIDIA A100 GPU. For the ground truth colour and albedo images, we preprocess them

to ensure that the intensities in linear space are within the range of  $[0,1]$ , and then we convert them to the logarithmic domain for improved numerical stability during training. For additional training details, please refer to Section B in the supplementary materials.

## 4 Experiments

We compare our method to the latest point-based inverse rendering techniques, namely GS-IR [13] and DPIR [4], across synthetic and real-world datasets. These datasets include the NeRF Synthetic dataset [17], PS-NeRF [26] (synthetic), and a subset of Tank & Temples [9] (real-world).

The baseline methods are initialized using their respective original strategies: visual hull for DPIR and Structure-from-Motion (SfM) for GS-IR, with each scene containing between 100,000 and 400,000 points in the end. In contrast, our method uses a significantly sparser point cloud of 30,000 points, which is initialized randomly.

### 4.1 Novel View Synthesis

We begin by evaluating models’ performances for novel view synthesis using the PSNR, SSIM, and LPIPS [31] metrics. Table 1 summarizes the average rendering reconstruction quality compared to baseline methods across synthetic and real-world datasets. Detailed scene breakdowns can be found in the supplementary materials. Our method consistently outperforms both inverse rendering baselines and the original PAPR across all metrics for both synthetic and real-world datasets. These results demonstrate the superior rendering quality of our method for novel view synthesis.

	Synthetic			Real-world			Initialization
	PSNR $\uparrow$	SSIM $\uparrow$	LPIPS <sub>v<sub>gg</sub></sub> $\downarrow$	PSNR $\uparrow$	SSIM $\uparrow$	LPIPS <sub>v<sub>gg</sub></sub> $\downarrow$	
DPIR [4]	26.18	0.865	0.084	19.15	0.857	0.188	Visual Hull
GS-IR [13]	29.88	0.943	0.059	26.25	0.905	0.102	SfM
PAPR [32]	32.07	0.971	0.038	28.72	0.940	0.097	Random
<i>Intrinsic PAPR (Ours)</i>	<b>33.55</b>	<b>0.982</b>	<b>0.023</b>	<b>29.75</b>	<b>0.952</b>	<b>0.082</b>	Random

Table 1: Evaluating novel view synthesis and image quality metrics (PSNR, SSIM and LPIPS [31]) on synthetic (NeRF Synthetic [17] and PS-NeRF [26]) and real-world (Tanks & Temples subset [9]) datasets. Higher PSNR and SSIM scores are better, while lower LPIPS scores are better. Our method outperforms the baselines across all metrics on both datasets.

	Albedo Transfer Error $\downarrow$			Comp. Feat. Decoupling Error $\downarrow$			Surface Details Preservation Error $\downarrow$		
	Ours	GS-IR	DPIR	Ours	GS-IR	DPIR	Ours	GS-IR	DPIR
<i>Lego</i>	<b>9.54</b>	30.31	21.18	<b>4.82</b>	18.14	18.95	<b>804.41</b>	1560.43	1872.29
<i>Materials</i>	<b>13.37</b>	31.46	22.18	<b>7.50</b>	25.32	33.87	<b>966.18</b>	1029.31	1180.79
<i>Hotdog</i>	<b>4.98</b>	15.53	8.83	<b>0.97</b>	26.53	5.22	<b>361.82</b>	606.87	573.24

Table 2: **Evaluating Point-level Albedo Transfer:** This table includes a comparison of the albedo transfer performance. The transfer error is calculated using the  $L_2$  distance between the albedo feature of the source and target points. For albedo-shading decoupling, we measure the  $L_2$  distance of shading intensity on the target area before and after the transfer. To assess surface detail preservation, we report the  $L_2$  distance on the edge maps of the target area before and after the transfer. Smaller error values indicate a more successful transfer. As shown, our method outperforms all baselines (GS-IR [13], DPIR [4]) across all scenes presented in Figure 4

### 4.2 Point-level Albedo and Shading Editing

We proceed with evaluating the models’ performances on point-level albedo and shading editing. To ensure a fair comparison of albedo and shading editing quality across methods, we conduct a transfer evaluation where the albedo/shading from one source point is transferred to a target region in the scene. Effective editing should excel along the following axes:

- (a) **Accuracy:** The editing should accurately reflect the source’s attributes being transferred in the target region, ensuring faithful albedo/shading transfer.
- (b) **Shading-Albedo Feature Decoupling:** During a transfer, the albedo and shading features need to be completely decoupled, in both the source

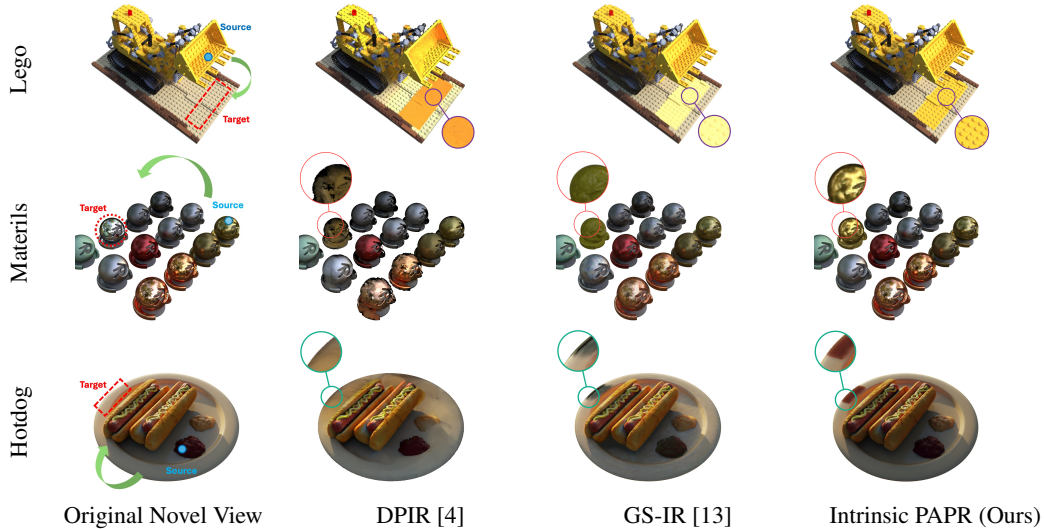


Figure 4: **Point-level Albedo Transfer**: Qualitative comparison of point-level albedo transfer on the NeRF synthetic dataset [17]. Our method effectively transfers the albedo from a source point (marked in blue) to target points (marked in red) by transferring its albedo feature vector. This transfer maintains the surface details and optical properties of the target region. Furthermore, our method ensures that the shading intensity at the target region remains unaffected by the shading at the source point. In contrast, the latest inverse rendering baselines struggle to transfer the correct colour (Lego, Hotdog), lose surface details (Lego, Materials) and optical properties like reflectivity (Materials), and fail to preserve shading at the target regions post-transfer (Hotdog).

	Shading Transfer Error ↓			Comp. Feat. Decoupling Error ↓			Surface Details Preservation Error ↓		
	Ours	GS-IR	DPIR	Ours	GS-IR	DPIR	Ours	GS-IR	DPIR
<i>Lego</i>	<b>14.39</b>	38.56	57.71	<b>7.24</b>	10.76	14.15	<b>322.69</b>	415.30	666.96
<i>Chair</i>	<b>6.55</b>	20.18	11.31	<b>3.28</b>	5.39	6.56	<b>45.72</b>	65.32	183.48
<i>Hotdog</i>	<b>2.43</b>	19.57	5.21	<b>0.79</b>	2.45	1.19	<b>93.74</b>	144.09	230.42

Table 3: **Evaluating Point-level Shading Transfer**: This table compares the effectiveness of shading transfer between our method and baselines. The transfer error is determined by calculating the  $L_2$  distance between the shading features of the source and target points. To evaluate albedo-shading decoupling, we measure the  $L_2$  distance of the albedo in the target area before and after the transfer. Surface detail preservation is assessed by comparing the  $L_2$  distance of the edge maps in the target area before and after the transfer. Smaller error values signify a more successful transfer. As shown, our method outperforms all baselines (GS-IR [13], DPIR [4]) across all scenes presented in Figure 5.

point and target points. Otherwise, the complementary features of the source (shading for albedo transfers and vice versa) point will be applied to the target region and/or unwanted complementary features of the target region will affect the transferred features. **(c) Preservation**: The editing should maintain the original surface details and optical properties of the target area, including reflectivity, translucency, and transparency, during transfers.

To quantitatively measure (a) Accuracy and (b) Shading-Albedo Feature Decoupling, we use a recent diffusion-based model [11] to decompose the rendered images before and after the transfer into albedo and shading components, denoted as  $(A_I, S_I)$  and  $(A_T, S_T)$  respectively. Next, we project the source and target points onto the image plane to determine the locations of the corresponding pixels. To measure the transfer error, we calculate the  $L_2$  distance for the transferred feature (albedo/shading) between the source and target pixels in the respective image ( $A_T$  for albedo transfer and  $S_T$  for shading transfer). To evaluate shading-albedo feature decoupling, we compute the  $L_2$  distance of the complementary feature on the target pixels before and after the transfer (albedo  $d(A_I, A_T)$  for shading transfer and vice versa). For surface detail preservation, we apply the Sobel edge detection operator to obtain edge maps of both the original and transferred images, then calculate the  $L_2$  distance between these edge maps.

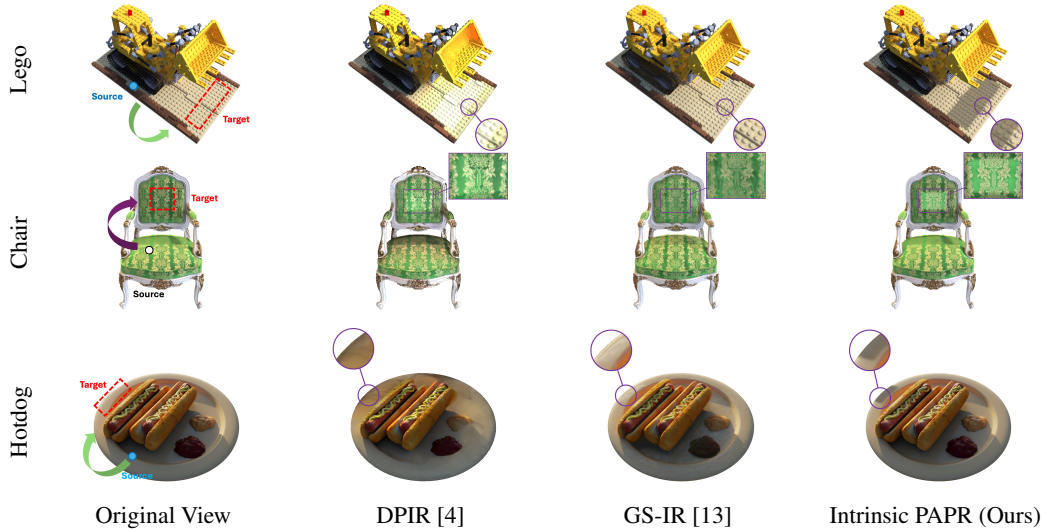


Figure 5: **Point-level Shading Transfer**: Qualitative comparison of point-level shading transfer on the NeRF synthetic dataset [17]. Our method demonstrates effective shading transfer from a source point (marked in blue) to target points (marked in red) by transferring its shading feature vector. Importantly, our method preserves the albedo at the target region without introducing the albedo from the source point. This highlights our method’s capability to encode distinct information in albedo and shading features. In contrast, GS-IR [13] struggles to accurately transfer shading values from the source, resulting in a similar appearance to the original view and introducing high-frequency noise (Lego, Hotdog, Chair). DPIR [4] also inaccurately transfers shading and fails to decouple shading from albedo in the source point, leading to undesired changes in the albedo of the target area (Lego).

#### 4.2.1 Point-level Albedo Transfer

To perform point-level albedo transfer in our method, we copy the albedo feature vector from the selected point to the albedo feature vectors of points in the target region. Subsequently, we render the novel view using the modified point feature vectors. A similar process is also applied to the baseline methods. DPIR [4] utilizes a feature vector for each point, passing them through a diffuse albedo network to represent each point’s albedo. This allows copying and replacing albedo features between points. GS-IR [13] follows a similar approach, using an albedo vector for each splat.

As shown in Figure 4 and Table 2, DPIR and GS-IR struggle with albedo transfer, introducing noise and distorting the target surface while mixing shading and albedo features. In contrast, our model accurately transfers the correct albedo, preserves target surface details and optical properties, and clearly separates albedo and shading features, achieving a more realistic result. Additional results for synthetic, and real-world scenes, as well as a video demonstrating the 360-degree rendering of the editing results, are included in the supplementary materials.

#### 4.2.2 Point-level Shading Transfer

Similar to point-level albedo transfer, we apply shading transfer using our method by copying the shading feature vector of a source point to the shading feature vectors of the points at the target region. DPIR [4] processes each point’s features through two networks—the specular basis coefficient network and the specular basis network—to calculate point specularity. For shading transfer, we swap the target area’s calculated specularity with that of the source point. Shading model in GS-IR [13] is influenced by the metallic and roughness values. Before rendering, we replace the target points’ metallic and roughness values with those from the source point.

As shown in Figure 5 and Table 3, DPIR and GS-IR often fail to accurately transfer the correct shading level from the source, resulting in inadequate shading transfer accuracy. In addition, their results show signs of albedo leakage which indicates poor decoupling of the albedo and shading. In contrast, our method successfully transfers the source shading while preserving the target area’s albedo, surface details, and optical properties. This highlights our model’s effectiveness in accurately

learning and decoupling shading and albedo features for each point. Additional results for synthetic and real-world scenes, as well as a video demonstrating the 360-degree rendering of the editing results, are included in the supplementary materials.

### 4.2.3 Additional Albedo and Shading Editing Techniques

In this section, we present additional albedo and shading editing capabilities enabled by our method, which go beyond simple transfers from other regions within the same scene.

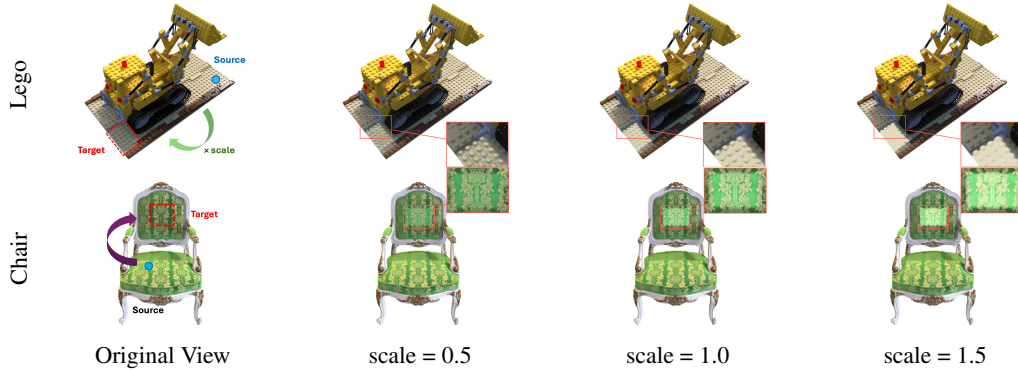


Figure 6: **Point-level Shading Intensity Control:** We control the intensity of the transferred shading from a source point (marked in blue) to a target region (marked in red) by scaling. Decreasing the scaling reduces shading intensity, while increasing the scaling increases shading intensity.

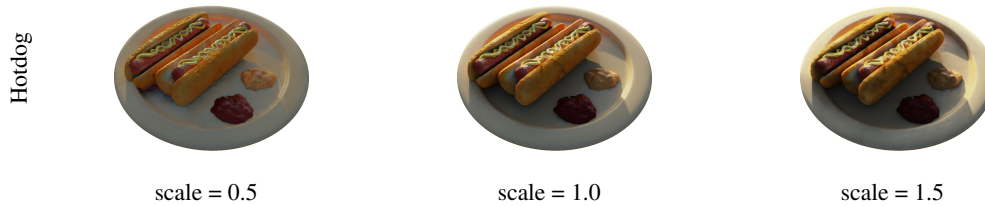


Figure 7: **Scene-level Shading Intensity Control:** We manipulate the overall scene shading by adjusting the scaling factor applied to the shading feature vectors of all points. Decreasing this scaling reduces contrast, while increasing it enhances the contrast within the scene.

**Point-level and Scene-level Shading Editing with Intensity Control:** We showcase our method’s capability to edit shading by scaling the shading feature vectors. Figure 6 illustrates point-level control, where the shading feature vector of the source point is scaled before transferring to the target point. Additionally, Figure 7 demonstrates scene-level shading editing by scaling the shading feature vectors of all points. These experiments highlight that a point’s shading intensity directly corresponds

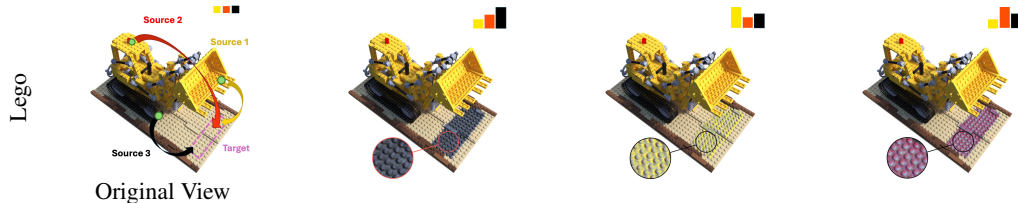


Figure 8: We demonstrate our method’s capability to generate novel colours within the scene by combining albedo feature vectors from distinct source points. The leftmost figure displays the three selected source points, each with yellow, red, and black albedo colours. The subsequent figures illustrate the newly created colours in the target region, achieved by different weighted combinations of the albedo features. This highlights the flexibility of our method in point-level albedo editing compared to simply transferring existing colours within the scene.

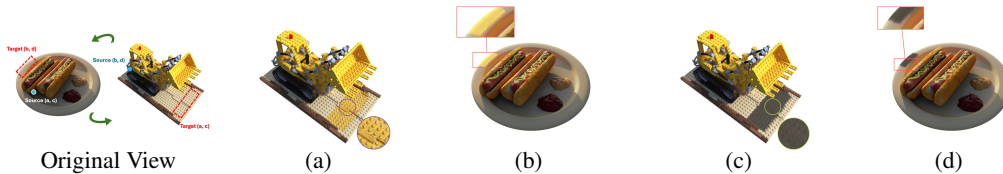


Figure 9: **Cross-Scene Shading and Albedo Transfer:** We demonstrate our method’s effectiveness in transferring point-level albedo and shading between different scenes. The models on two distinct scenes are trained jointly while sharing certain model components. In (a), we transfer the albedo from the Hotdog bun to the Lego board; in (b), the albedo from the Lego body to the Hotdog plate. Additionally, in (c), we transfer shading from the Hotdog plate to the Lego board, and in (d), shading from the Lego’s track to the Hotdog plate. The transferred albedo and shading closely match those of the source points, showcasing precise transfer capabilities across scenes.

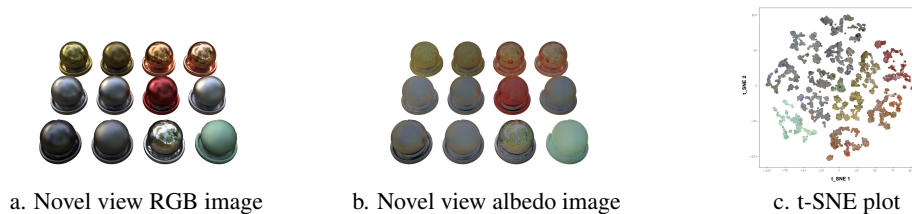


Figure 10: **t-SNE Visualization of Albedo Features:** This figure showcases the results of (a) our RGB rendering and (b) the predicted albedo for a novel viewpoint. In (c), we present a t-SNE visualization of the high-dimensional albedo features. Each point in the t-SNE plot is colour-coded based on its corresponding albedo value in the predicted albedo image. The t-SNE plot reveals distinct clusters representing different colour variations in the albedo feature.

to the magnitude of its shading features, enabling precise control over shading intensity through scaling. Additional results can be found in the supplementary materials.

**Colour Creation via Albedo Feature Combination:** Figure 8 highlights our method’s ability to create novel colours within a scene by combining the albedo features from different points. This result showcases the potential for editing novel colours while preserving details in the target regions.

Moreover, Figure 10 presents the t-SNE visualization of the learnt albedo features in the Materials scene. This visualization illustrates how similar albedo features cluster into distinct groups, reflecting similar colours. Additional t-SNE results can be found in the supplementary materials.

**Cross-Scene Shading and Albedo Transfer:** We jointly train two models on two distinct scenes by sharing certain model components (see the supplementary section B.3 for more details). Figure 9 illustrates the transfer of albedo and shading between scenes, showcasing the potential of our model for flexible albedo and shading editing.

## 5 Discussion and Conclusion

**Limitation** While our method demonstrates promising results, it does have certain limitations that open avenues for future work. Specifically, the reliance on a pretrained model to obtain ground-truth albedo may propagate biases present in the pretraining data, potentially affecting the accuracy and generalizability of our results.

**Societal Impact** The demonstrated editing capabilities could significantly assist artists in achieving albedo and shading editing of 3D scenes more effectively. These use cases may range from digitally created synthetic scenes to real-world scenes captured by mobile devices. However, this ease of editing could also lead to increased unauthorized copying and manipulation of 3D content, raising copyright and intellectual property concerns.

**Conclusion** In this paper, we introduce “Intrinsic PAPR”, a novel method for point-level 3D scene albedo and shading editing. Building on the Proximity Attention Point Rendering (PAPR) technique, our approach effectively models the decomposition of a 3D scene into albedo and shading components, enabling detailed and consistent editing across different viewpoints.

**Acknowledgements** This research was enabled in part by support provided by NSERC, the BC DRI Group and the Digital Research Alliance of Canada.

## References

- [1] Chris Careaga and Yagiz Aksoy. Intrinsic image decomposition via ordinal shading. *ACM Transactions on Graphics*, 43:1 – 24, 2023.
- [2] Anpei Chen, Zexiang Xu, Andreas Geiger, Jingyi Yu, and Hao Su. Tensorf: Tensorial radiance fields. In *European Conference on Computer Vision*, 2022.
- [3] Hoon-Gyu Chung, Seokjun Choi, and Seung-Hwan Baek. Differentiable point-based inverse rendering. *ArXiv*, abs/2312.02480, 2023.
- [4] Hoon-Gyu Chung, Seokjun Choi, and Seung-Hwan Baek. Differentiable point-based inverse rendering. In *Proceedings of the IEEE/CVF Conference on Computer Vision and Pattern Recognition (CVPR)*, 2024.
- [5] Partha Das, Sezer Karaoglu, and Theo Gevers. Pie-net: Photometric invariant edge guided network for intrinsic image decomposition. *2022 IEEE/CVF Conference on Computer Vision and Pattern Recognition (CVPR)*, pages 19758–19767, 2022.
- [6] Haian Jin, Isabella Liu, Peijia Xu, Xiaoshuai Zhang, Songfang Han, Sai Bi, Xiaowei Zhou, Zexiang Xu, and Hao Su. Tensorf: Tensorial inverse rendering. *2023 IEEE/CVF Conference on Computer Vision and Pattern Recognition (CVPR)*, pages 165–174, 2023.
- [7] Bernhard Kerbl, Georgios Kopanas, Thomas Leimkühler, and George Drettakis. 3d gaussian splatting for real-time radiance field rendering. *ACM Transactions on Graphics*, 42(4), 2023.
- [8] Diederik P. Kingma and Jimmy Ba. Adam: A method for stochastic optimization. *CoRR*, abs/1412.6980, 2014.
- [9] Arno Knapitsch, Jaesik Park, Qian-Yi Zhou, and Vladlen Koltun. Tanks and temples: Benchmarking large-scale scene reconstruction. *ACM Transactions on Graphics*, 36(4), 2017.
- [10] Christoph Lassner and Michael Zollhöfer. Pulsar: Efficient sphere-based neural rendering. *2021 IEEE/CVF Conference on Computer Vision and Pattern Recognition (CVPR)*, pages 1440–1449, 2021.
- [11] Hsin-Ying Lee, Hung-Yu Tseng, Hsin-Ying Lee, and Ming-Hsuan Yang. Exploiting diffusion prior for generalizable dense prediction, 2024.
- [12] Zhengqin Li, Mohammad Shafiei, Ravi Ramamoorthi, Kalyan Sunkavalli, and Manmohan Chandraker. Inverse rendering for complex indoor scenes: Shape, spatially-varying lighting and svbrdf from a single image. *2020 IEEE/CVF Conference on Computer Vision and Pattern Recognition (CVPR)*, pages 2472–2481, 2019.
- [13] Zhihao Liang, Qi Zhang, Ying Feng, Ying Shan, and Kui Jia. Gs-ir: 3d gaussian splatting for inverse rendering. *arXiv preprint arXiv:2311.16473*, 2023.
- [14] Zhihao Liang, Qi Zhang, Yingfa Feng, Ying Shan, and Kui Jia. Gs-ir: 3d gaussian splatting for inverse rendering. *ArXiv*, abs/2311.16473, 2023.
- [15] Yunfei Liu, Yu Li, Shaodi You, and Feng Lu. Unsupervised learning for intrinsic image decomposition from a single image. *2020 IEEE/CVF Conference on Computer Vision and Pattern Recognition (CVPR)*, pages 3245–3254, 2019.
- [16] Jundan Luo, Zhaoyang Huang, Yijin Li, Xiaowei Zhou, Guofeng Zhang, and Hujun Bao. Niid-net: Adapting surface normal knowledge for intrinsic image decomposition in indoor scenes. *IEEE Transactions on Visualization and Computer Graphics*, 26:3434–3445, 2020.
- [17] Ben Mildenhall, Pratul P. Srinivasan, Matthew Tancik, Jonathan T. Barron, Ravi Ramamoorthi, and Ren Ng. Nerf: Representing scenes as neural radiance fields for view synthesis. *ArXiv*, abs/2003.08934, 2020.

- [18] Thomas Müller, Alex Evans, Christoph Schied, and Alexander Keller. Instant neural graphics primitives with a multiresolution hash encoding. *ACM Transactions on Graphics (TOG)*, 41:1 – 15, 2022.
- [19] Takuya Narihira, Michael Maire, and Stella X. Yu. Learning lightness from human judgement on relative reflectance. *2015 IEEE Conference on Computer Vision and Pattern Recognition (CVPR)*, pages 2965–2973, 2015.
- [20] Julian Ost, Issam Hadj Laradji, Alejandro Newell, Yuval Bahat, and Felix Heide. Neural point light fields. *2022 IEEE/CVF Conference on Computer Vision and Pattern Recognition (CVPR)*, pages 18398–18408, 2021.
- [21] K. Sarkar, Marcel C. Bühler, Gengyan Li, Daoye Wang, Delio Vicini, Jérémy Riviere, Yinda Zhang, Sergio Orts-Escolano, Paulo F. U. Gotardo, Thabo Beeler, and Abhimitra Meka. Lit-nerf: Intrinsic radiance decomposition for high-quality view synthesis and relighting of faces. *SIGGRAPH Asia 2023 Conference Papers*, 2023.
- [22] Soumyadip Sengupta, Jinwei Gu, Kihwan Kim, Guilin Liu, David W. Jacobs, and Jan Kautz. Neural inverse rendering of an indoor scene from a single image. *2019 IEEE/CVF International Conference on Computer Vision (ICCV)*, pages 8597–8606, 2019.
- [23] Pratul P. Srinivasan, Boyang Deng, Xiuming Zhang, Matthew Tancik, Ben Mildenhall, and Jonathan T. Barron. Nerv: Neural reflectance and visibility fields for relighting and view synthesis. *2021 IEEE/CVF Conference on Computer Vision and Pattern Recognition (CVPR)*, pages 7491–7500, 2020.
- [24] Xiaoyan Xing, Konrad Groh, Sezer Karaoglu, and Theo Gevers. Intrinsic image decomposition using point cloud representation. 2023.
- [25] Qiangeng Xu, Zexiang Xu, Julien Philip, Sai Bi, Zhixin Shu, Kalyan Sunkavalli, and Ulrich Neumann. Point-nerf: Point-based neural radiance fields. *2022 IEEE/CVF Conference on Computer Vision and Pattern Recognition (CVPR)*, pages 5428–5438, 2022.
- [26] Wenqi Yang, Guanying Chen, Chaofeng Chen, Zhenfang Chen, and Kwan-Yee K. Wong. Ps-nerf: Neural inverse rendering for multi-view photometric stereo. In *European Conference on Computer Vision (ECCV)*, 2022.
- [27] Weicai Ye, Shuo Chen, Chong Bao, Hujun Bao, Marc Pollefeys, Zhaopeng Cui, and Guofeng Zhang. Intrinsicnerf: Learning intrinsic neural radiance fields for editable novel view synthesis. *2023 IEEE/CVF International Conference on Computer Vision (ICCV)*, pages 339–151, 2022.
- [28] Alex Yu, Sara Fridovich-Keil, Matthew Tancik, Qinhong Chen, Benjamin Recht, and Angjoo Kanazawa. Plenoxels: Radiance fields without neural networks. *2022 IEEE/CVF Conference on Computer Vision and Pattern Recognition (CVPR)*, pages 5491–5500, 2021.
- [29] Kai Zhang, Fujun Luan, Qianqian Wang, Kavita Bala, and Noah Snavely. Physg: Inverse rendering with spherical gaussians for physics-based material editing and relighting. *2021 IEEE/CVF Conference on Computer Vision and Pattern Recognition (CVPR)*, pages 5449–5458, 2021.
- [30] Qian Zhang, Seung-Hwan Baek, Szymon Rusinkiewicz, and Felix Heide. Differentiable point-based radiance fields for efficient view synthesis. *SIGGRAPH Asia 2022 Conference Papers*, 2022.
- [31] Richard Zhang, Phillip Isola, Alexei A. Efros, Eli Shechtman, and Oliver Wang. The unreasonable effectiveness of deep features as a perceptual metric. *2018 IEEE/CVF Conference on Computer Vision and Pattern Recognition*, pages 586–595, 2018.
- [32] Yanshu Zhang, Shichong Peng, Alireza Moazeni, and Ke Li. Papr: Proximity attention point rendering, 2023.
- [33] Yuanqing Zhang, Jiaming Sun, Xingyi He He, Huan Fu, Rongfei Jia, and Xiaowei Zhou. Modeling indirect illumination for inverse rendering. *2022 IEEE/CVF Conference on Computer Vision and Pattern Recognition (CVPR)*, pages 18622–18631, 2022.

- [34] Hao Zhou, Xiang Yu, and David W. Jacobs. Glosh: Global-local spherical harmonics for intrinsic image decomposition. *2019 IEEE/CVF International Conference on Computer Vision (ICCV)*, pages 7819–7828, 2019.
- [35] Tinghui Zhou, Philipp Krähenbühl, and Alexei A. Efros. Learning data-driven reflectance priors for intrinsic image decomposition. *2015 IEEE International Conference on Computer Vision (ICCV)*, pages 3469–3477, 2015.
- [36] Rui Zhu, Zhengqin Li, Janarbek Matai, Fatih Murat Porikli, and Manmohan Chandraker. Irisformer: Dense vision transformers for single-image inverse rendering in indoor scenes. *2022 IEEE/CVF Conference on Computer Vision and Pattern Recognition (CVPR)*, pages 2812–2821, 2022.
- [37] Daniel Zoran, Phillip Isola, Dilip Krishnan, and William T. Freeman. Learning ordinal relationships for mid-level vision. *2015 IEEE International Conference on Computer Vision (ICCV)*, pages 388–396, 2015.
- [38] Yiming Zuo and Jia Deng. View synthesis with sculpted neural points. *ArXiv*, abs/2205.05869, 2022.

## A Appendix / supplemental material

### A.1 Overview Video

Please refer to the supplementary videos.zip file for 360-degree editing results on albedo and shading transfers explained in the experiment section.

## B Implementation Details

### B.1 Proximity Attention

Followed by the attention mechanism introduced in PAPR [32] to filter the top  $K$  nearest points  $\mathbf{p}_i$  for a given ray  $\mathbf{r}_j$ , our attention component includes four independent MLPs ( $f_{\theta_K}$ ,  $f_{\theta_{V_A}}$ ,  $f_{\theta_{V_S}}$ , and  $f_{\theta_Q}$ ) to calculate the key  $\mathbf{k}_{i,j}$ , the value  $\mathbf{v}_{i,j}$  (based on albedo and shading values), and the query  $\mathbf{q}_j$  for the attention mechanism. Figure 11 illustrates these four MLPs.

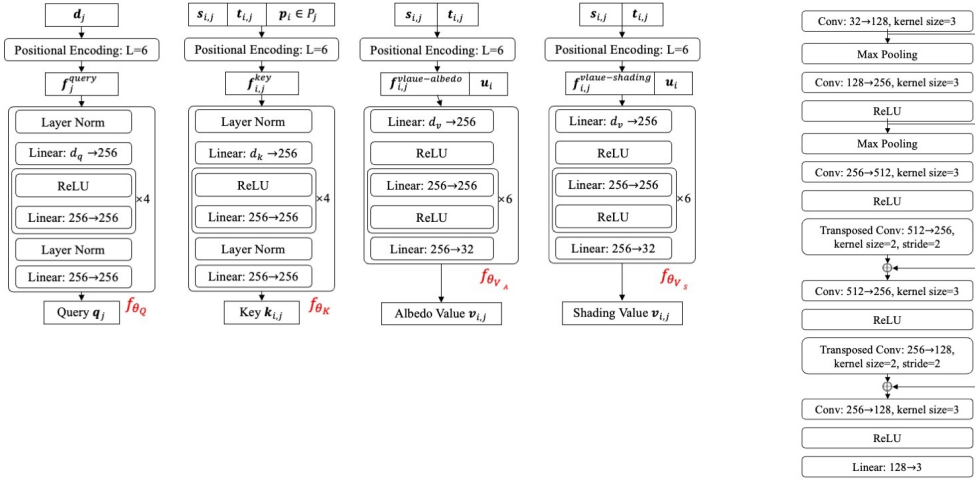


Figure 12: U-Net details.

Figure 11: Embedding MLPs architecture details.

	Chair	Drums	Ficus	Hotdog	Lego	Materials	Mic	Ship	Moneki	Avg.
PSNR $\uparrow$										
<i>DPIR</i> [4]	26.10	23.15	24.53	25.43	27.35	26.39	27.33	25.49	29.88	26.18
<i>GS-IR</i> [13]	31.10	24.50	30.77	33.81	32.79	25.79	31.68	26.73	31.73	29.88
<i>PAPR</i> [32]	33.59	25.35	36.50	36.40	32.62	29.54	35.64	26.92	32.10	32.07
<i>Intrinsic PAPR (Ours)</i>	<b>35.76</b>	<b>27.58</b>	<b>37.97</b>	<b>36.72</b>	<b>34.50</b>	<b>30.96</b>	<b>36.21</b>	<b>27.39</b>	<b>34.83</b>	<b>33.55</b>
SSIM $\uparrow$										
<i>DPIR</i> [4]	0.822	0.864	0.813	0.805	0.798	0.861	0.946	0.937	0.939	0.865
<i>GS-IR</i> [13]	0.964	0.927	0.965	0.967	0.962	0.912	0.970	0.857	0.964	0.943
<i>PAPR</i> [32]	0.986	0.951	0.994	0.988	0.981	0.972	0.993	0.904	0.972	0.971
<i>Intrinsic PAPR (Ours)</i>	<b>0.991</b>	<b>0.975</b>	<b>0.996</b>	<b>0.992</b>	<b>0.990</b>	<b>0.974</b>	<b>0.997</b>	<b>0.936</b>	<b>0.992</b>	<b>0.982</b>
LPIPS $_{V_{gg}}\downarrow$										
<i>DPIR</i> [4]	0.122	0.145	0.279	0.136	0.140	0.121	0.132	0.113	0.009	0.084
<i>GS-IR</i> [13]	0.030	0.064	0.028	0.049	0.035	0.079	0.031	0.150	0.068	0.059
<i>PAPR</i> [32]	0.018	0.055	0.010	0.021	0.027	0.036	0.007	0.129	0.043	0.038
<i>Intrinsic PAPR (Ours)</i>	<b>0.013</b>	<b>0.033</b>	<b>0.005</b>	<b>0.012</b>	<b>0.013</b>	<b>0.020</b>	<b>0.006</b>	<b>0.091</b>	<b>0.012</b>	<b>0.023</b>

Table 4: Comparison of image quality metrics (PSNR, SSIM and LPIPS [31]), broken down by scene, for the NeRF Synthetic [17] and PS-NeRF [26].

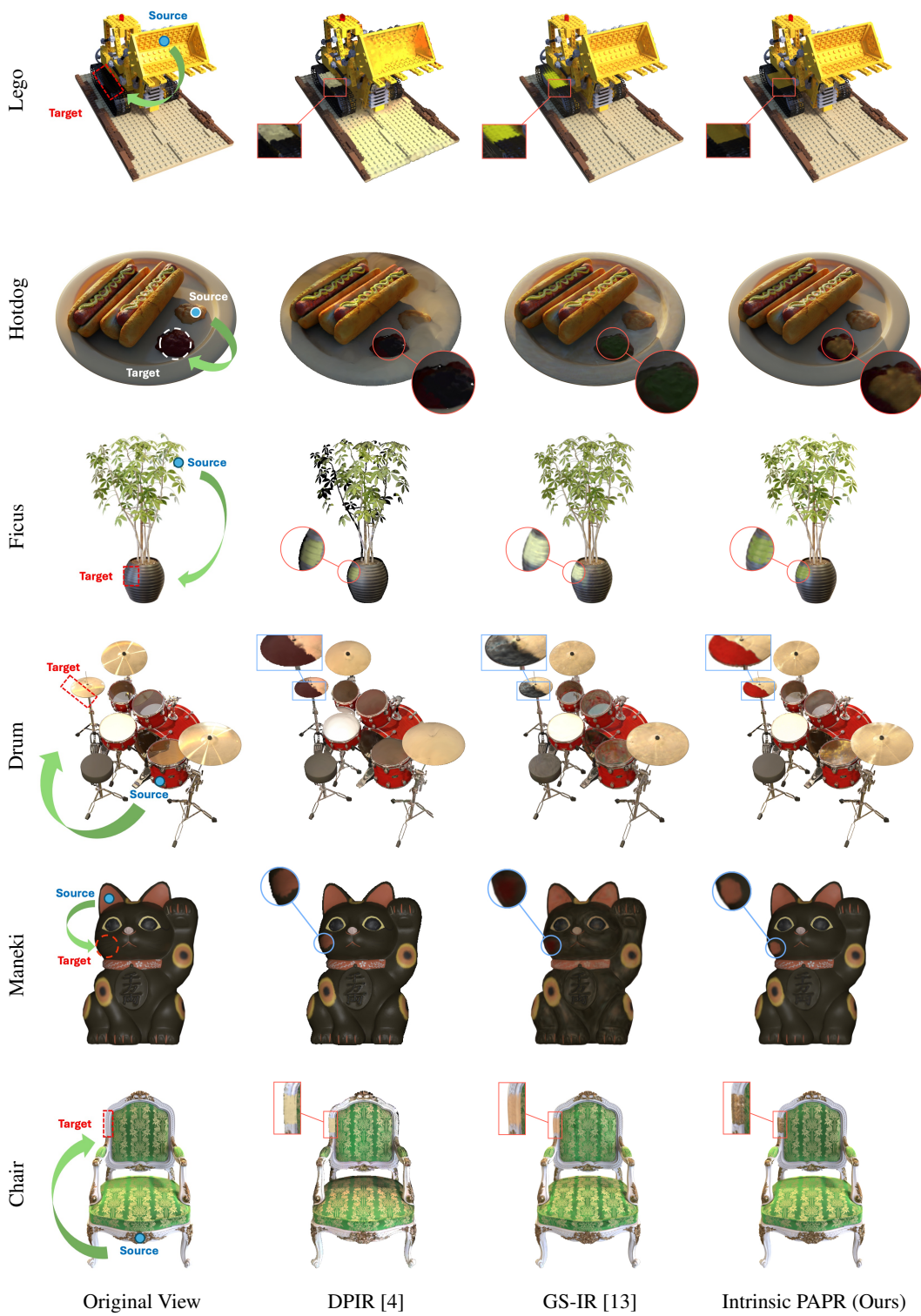


Figure 13: **Point-level Albedo Transfer**: Extra comparisons for novel view albedo editing method on the NeRF Synthetic [17] and PS-NeRF [26]

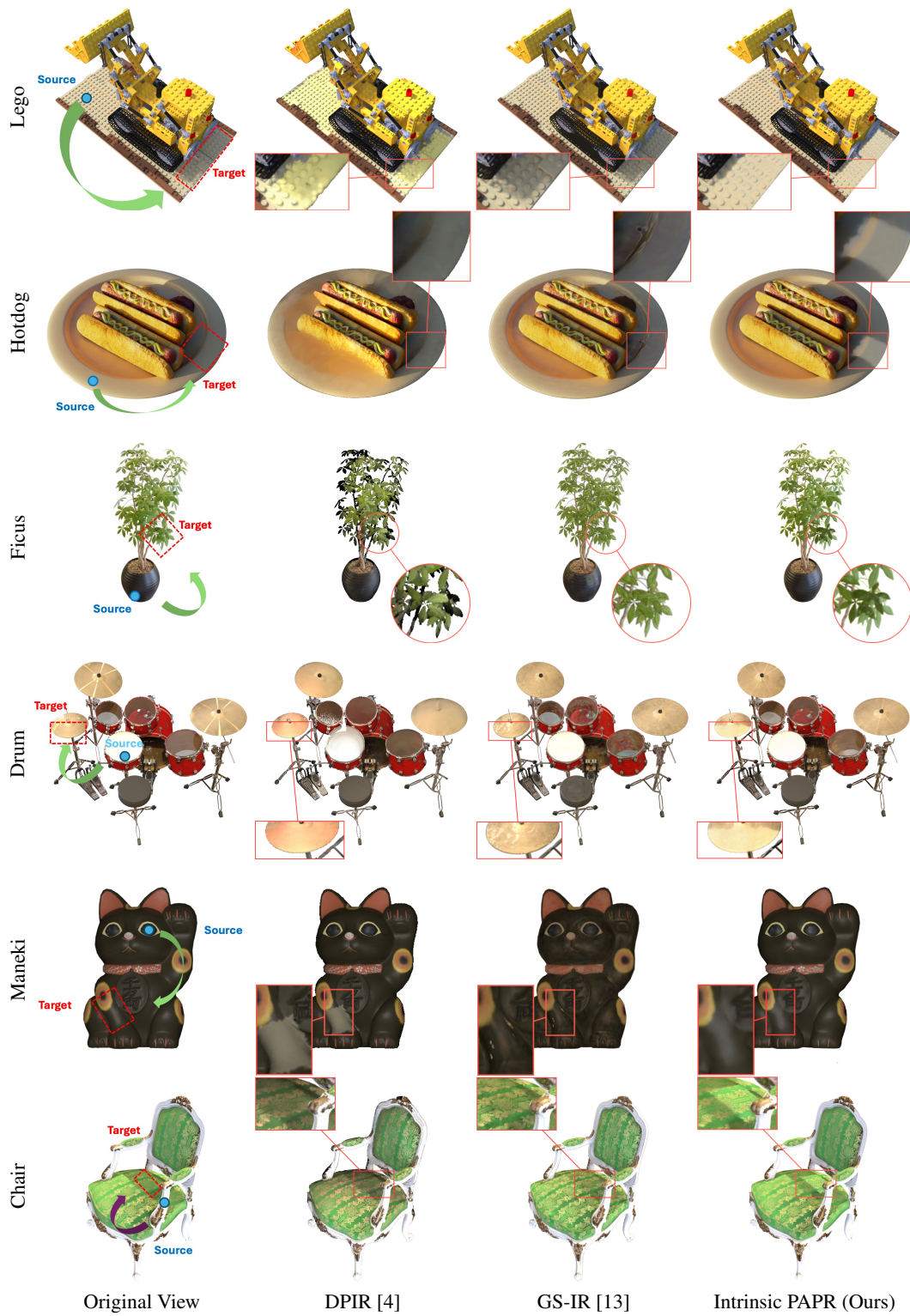
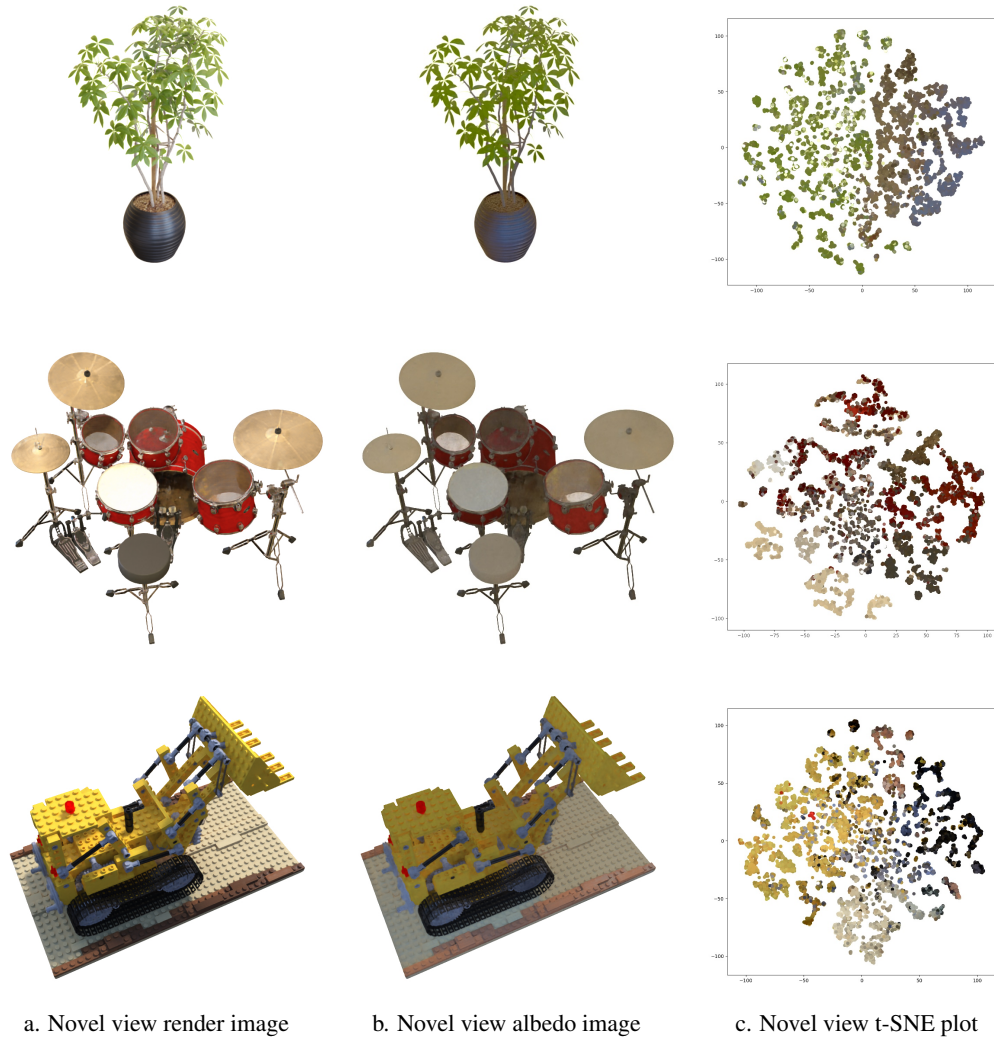


Figure 14: **Point-level Shading Transfer**: Extra comparisons for novel view shading editing method on the NeRF Synthetic [17] and PS-NeRF [26].



**Figure 15: Scene-level Shading Intensity Control:** This figure showcases our method’s capability to control the overall shading intensity of an image. By building on our point-level shading adjustment technique, we can now modify the shading intensity across the entire image. This is accomplished by scaling the magnitude of shading features for all points in the image by a consistent factor. Decreasing the scaling factor reduces contrast, while increasing it enhances the contrast within the scene.



**Figure 16: t-SNE Visualization of High-dimensional Albedo Features:** This figure displays additional results of our rendering and albedo prediction for a novel view, with panels (a) and (b) respectively. Panel (c) shows a t-SNE visualization of the high-dimensional albedo features, where points are coloured according to their corresponding albedo values in the predicted albedo image. This highlights how similar albedo features cluster together in lower-dimensional space and demonstrates clear separation between clusters representing different albedo features.



Figure 17: **Point-level Albedo Editing**: Comparisons for novel view albedo editing method on the Tanks & Temples subset [9].



Figure 18: **Point-level Shading Editing**: Comparisons for novel view shading editing method on the Tanks & Temples subset [9].

	Family	Truck	Caterpillar	Ignatius	Barn	Avg.
PSNR $\uparrow$						
<i>DPIR</i> [4]	19.86	18.70	19.17	18.18	19.87	19.15
<i>GS-IR</i> [13]	30.16	25.84	23.47	26.24	25.52	26.25
<i>PAPR</i> [32]	34.39	26.98	<b>26.79</b>	28.40	27.06	28.72
<i>Intrinsic PAPR (Ours)</i>	<b>35.20</b>	<b>27.53</b>	26.57	<b>31.97</b>	<b>27.47</b>	<b>29.75</b>
SSIM $\uparrow$						
<i>DPIR</i> [4]	0.874	0.844	0.828	0.949	0.791	0.857
<i>GS-IR</i> [13]	0.961	0.909	0.878	0.920	0.857	0.905
<i>PAPR</i> [32]	0.983	0.931	0.932	0.956	<b>0.896</b>	0.940
<i>Intrinsic PAPR (Ours)</i>	<b>0.989</b>	<b>0.953</b>	<b>0.956</b>	<b>0.968</b>	0.893	<b>0.952</b>
LPIPS $_{Vgg}\downarrow$						
<i>DPIR</i> [4]	0.154	0.310	0.251	0.101	0.124	0.188
<i>GS-IR</i> [13]	0.043	<b>0.092</b>	0.115	0.079	0.179	0.102
<i>PAPR</i> [32]	0.072	0.108	0.157	0.118	<b>0.031</b>	0.097
<i>Intrinsic PAPR (Ours)</i>	<b>0.018</b>	0.101	<b>0.081</b>	<b>0.047</b>	0.161	<b>0.082</b>

Table 5: Comparison of image quality metrics (PSNR, SSIM and LPIPS [31]), broken down by scene, for the Tanks & Temples [9] subset.

## B.2 Point Feature Renderer

Following the U-Net architectural design mentioned in PAPR, we adapted similar U-Nets for both the albedo feature and colour image renderer illustrated in Figure 12.

## B.3 Cross-Scene Albedo and Shading editing

We extend our point-level albedo and shading editing to work across different scenes. To enable the transfer of a point’s albedo or shading features between two scenes, we jointly train their models by sharing the albedo and shading value MLPs, as well as the albedo feature renderer. This allows the model to learn transferable albedo and shading representations. After training, we follow the same steps as for single-scene editing: selecting a point in the desired area from the source scene and transferring the shading or albedo features to the target area points in the target scene. The modified features in the target scene are then used for rendering following the standard process explained in Figure 2. Figure 9 showcases successful albedo and shading transfer between Lego and hotdog scenes.

# C Additional Results

## C.1 Quantitative Evaluation on Synthetic Datasets

In Table 4 we present detailed scene breakdowns comparison on synthetic (NeRF Synthetic [17] and PS-NeRF [26])

## C.2 Quantitative Evaluation on Real-world Dataset

In Table 5 we present detailed scene breakdowns comparison on Tanks & Temples subset [9].

## C.3 Point-level Albedo Transfer

We present additional qualitative results for the point-level albedo transfer task here. Figure 13 showcases transfers on the NeRF Synthetic dataset [17], while Figure 17 demonstrates real-world albedo editing on the Tanks and Temples [9] subset.

#### **C.4 Point-level Shading Transfer**

To further showcase our method’s capabilities, we include qualitative results for point-level shading transfer. Figure 14 demonstrates shading edits on the NeRF Synthetic dataset [17]. Meanwhile, Figure 18 highlights real-world applicability with shading edits on the Tanks and Temples [9] subset.

#### **C.5 Scene-level Shading Intensity Control**

In Figure 15 we present more examples of how our method is able to adjust the overall intensity of shading in a scene.

#### **C.6 t-SNE Visualization of High-dimensional Albedo Features**

In Figure 16 we present more showcases on the visualization of latent albedo features.